Nanoscale

PAPER

View Article Online
View Journal | View Issue

Check for updates

Cite this: *Nanoscale*, 2023, **15**, 7329

Tuning of electron transport layers using MXene/metal–oxide nanocomposites for perovskite solar cells and X-ray detectors†

Sajjad Hussain, ‡[a,b] Hailiang Liu, ‡[c] Dhanasekaran Vikraman, [d] Syed Hassan Abbas Jaffery,[a,b] Ghazanfar Nazir,[b] Faisal Shahzad, [e] Khalid Mujasam Batoo, [f] Jongwan Jung, [a,b] Jungwon Kang*[c] and Hyun-Seok Kim *[d]

Received 15th March 2023,
Accepted 15th March 2023

DOI: 10.1039/d3nr01196h

rsc.li/nanoscale

This work elaborates on the decoration of metal oxides (ZnO and Fe_3O_4) between MXene sheets for use as the supporting geometry of PCBM electron transport layers (ETLs) in perovskite solar cells and X-ray detectors. The metal oxide supports for carrying the plentiful charge carriers and the hydrophobic nature of MXenes provide an easy charge transfer path through their flakes and a smooth surface for the ETL. The developed interface engineering based on the MXene/ZnO and MXene/Fe_3O_4 hybrid ETL results in improved power conversion efficiencies (PCEs) of 13.31% and 13.79%, respectively. The observed PCE is improved to 25.80% and 30.34% by blending the MXene/ZnO and MXene/Fe_3O_4 nanoparticles with the PCBM layer, respectively. Various factors, such as surface modification, swift interfacial interaction, roughness decrement, and charge transport improvement, are strongly influenced to improve the device performance. Moreover, X-ray detectors with the MXene/Fe_3O_4-modulated PCBM ETL achieve a CCD-DCD, sensitivity, mobility, and trap density of 15.46 $\mu A\ cm^{-2}$, 4.63 mA per Gy per cm^2, $5.21 \times 10^{-4}\ cm^2\ V^{-1}\ s^{-1}$, and $1.47 \times 10^{15}\ cm^2\ V^{-1}\ s^{-1}$, respectively. Metal oxide-decorated MXene sheets incorporating the PCBM ETL are a significant route for improving the photoactive species generation, long-term stability, and high mobility of perovskite-based devices.

1. Introduction

Hybrid organic–inorganic halide perovskites, $CH_3NH_3PbX_3$ (X = I, Br, or Cl), have gained widespread interest as promising candidates for use as photoactive materials in solar cells and X-ray detector applications. This is owing to their outstanding electronic properties, such as their tunable bandgap, wide-range optical absorption, high ambipolar carrier transport properties, long carrier diffusion length, trivial exciton binding energy, and low-temperature processability and flexibility.[1–5] X-ray detectors have been used in diverse scientific applications, including medical equipment, optical communication, railway flaw detection, security checks, space/environmental exploration, and biosensing. Moreover, semiconductor-based direct X-ray detectors using amorphous selenium a-Se, HgI_2, InP, PbI_2, CdZnTe, CdSe, and CdTe have already been reported. However, their low carrier mobility, stability issues, high noise current, low absorption coefficient, and limited detection area restrict practical applications.[6–9] Organic–inorganic hybrid perovskites have attracted extensive research attention owing to their long electron–hole diffusion length, high mobility, low laser excitation threshold, and better quantum photoluminescence yield. Recently, lead halide perovskites have evolved as favorable semiconductors for X-ray detection owing to their excellent characteristics, such as high sensitivity, low detection limit, and large X-ray stopping power.[10,11] Similarly, halide perovskite hybrids realize outstanding optoelectronic properties and their unprecedented combination has improved solar cell development with more than 20% conversion efficiency.[12,13]

---

[a] *Hybrid Materials Center (HMC), Sejong University, Seoul 05006, Korea*
[b] *Department of Nanotechnology and Advanced Materials Engineering, Sejong University, Seoul 05006, Korea*
[c] *Convergence Semiconductor Research Center, Department of Electronics and Electrical Engineering, Dankook University, Yongin 16890, Korea. E-mail: jkang@dankook.ac.kr*
[d] *Division of Electronics and Electrical Engineering, Dongguk University-Seoul, Seoul 04620, Korea. E-mail: hyunseokk@dongguk.edu*
[e] *Department of Metallurgy and Materials Engineering, Pakistan Institute of Engineering and Applied Sciences (PIEAS), Islamabad, Pakistan*
[f] *King Abdullah Institute for Nanotechnology, King Saud University, Riyadh-11451, Saudi Arabia*

† Electronic supplementary information (ESI) available. See DOI: **https://doi.org/10.1039/d3nr01196h**

‡ These authors contributed equally.

In typical perovskite-based devices, a planar perovskite layer is embedded between a hole transfer layer (HTL) and an electron transfer layer (ETL) (ITO/HTL/perovskite layer/ETL/Au, Ag, or Al) in a gadget module to attract photon light and create electron–hole charge carriers. The transport layer(s) (HTL and ETL) and active perovskite layer play significant roles in improving the cell efficiency and stability. Moreover, the ETL is a vital layer in perovskite devices for charge transport, collection and extraction, eradicating electrical shunts between the perovskite and transparent electrode, and facilitating the trapping and recombination of charge carriers. The fullerene derivative, [6,6]-phenyl-C61-butyric acid methyl ester (PCBM), is the most conventional ETL for transporting electrons and effectively passivating any defects in the perovskite layer. However, there are many limitations to using the conventional PCBM ETL when fabricating perovskite devices. First, the uniformity of a PCBM ETL depends on the morphology beneath the perovskite active layer due to the larger size grain and rough or uneven nature of perovskites, which leave an opening or void. Second, during metal electrode deposition, hot metals permeate into them to develop direct interaction with the active layer perovskite, resulting to the neutralizing of excitons. Third, very thick PCBM ETLs produce a smooth surface that highly restrict the transportation and mobility (due to imbalanced light absorption efficiency) and scalable fabrication due to high cost.[14] Finally, PCBM is a hygroscopic material that is severely affected by moisture, which can degrade the robustness of perovskite-based devices. Many significant approaches have been implemented to enhance the enactment of perovskite devices by replacing or altering the PCBM ETL. Recently, metal oxide (MO) semiconductors including TiO_2, SnO_2, Cr_2O_3, CeO_2, Fe_3O_4, ZnO, Nb_2O_5, and Zn_2SnO_4 have been employed to replace or modify the PCBM layer.[15–19] In particular, modifying, doping, or multi-layer configurations of the ETL layer using MO semiconductors reduces the morphological defects, improves uniform coverage and rapid charge transport ability, and eliminates hysteresis characteristics, creating favorable band alignment, excellent interface contact, and visible transparency.[16,18,20]

Among these semiconductors, ZnO and Fe_3O_4, which are n-type semiconductors with a wide bandgap (2–3.5 eV), are promising ETLs in perovskite devices owing to their intrinsic properties including a high electron transport rate of 130–230 $cm^2\ V^{-1}\ s^{-1}$ and good chemical stability.[21,22] Lim *et al.* demonstrated surface-modified ZnO ETLs on flexible substrates with an average power conversion efficiency (PCE) of 11.9%.[23] Similarly, Hu *et al.* used hematite-based transportation films in perovskite-based solar cells that produced a PCE of 10.7%.[24] However, there are some intrinsic drawbacks of ZnO and Fe_3O_4. These include poor conductivity and severe charge recombination centers that trap photogenerated electrons due to surface defects and the presence of metal (Zn or Fe) and oxygen vacancies, which severely hinder local charge transfer.[25,26] Moreover, decomposition of the perovskite photoactive layer can easily corrode the Fe_3O_4 and ZnO ETL structures.[27] To overcome these critical problems, several researchers have attempted to improve the conductivity of the MO ETL to suppress the recombination and trapping of charge carriers between the perovskite active and ETL interface by modifying or replacing the ETL through dopants or hybridization.

Two-dimensional (2D) MXene-based materials have received significant attention because of their distinctive properties. These include outstanding intrinsic ionic or electronic conductivity (5000–10 000 S cm^{-1}) close to that of multi-layered graphenes, hydrophilicity, ease of processing with rich surface chemistry, excellent optical transparency, existing in semimetals, superconductors or semiconductors (based on the surface characteristics), high carrier density (3.8×10^{22} cm^{-3}), and superior mobility (1.0 $cm^2\ V^{-1}\ s^{-1}$).[28,29] Moreover, because of its charge carrier transference and gathering behaviors, MXenes have recently been used as both a HTL and an ETL to improve the efficiency and stability of PSCs.[30,31] However, these materials are still in their infancy and limitedly used in HTLs to check the progress for the practical application. Highly conducting materials have been hybridized with MO and used as HTLs and ETLs such as perylene bisimide,[32] nickel (Ni),[33] aluminum (Al),[34] and carbon-based derivatives (MXenes, graphenes, rGO, and CNTs).[35] Recently, Jayawardena *et al.*[36] and Hou *et al.*[25] have incorporated ZnO with rGO and MXene-$Ti_3C_2T_x$ to improve the PCE by providing charge extraction/collection channels between the ZnO nanoparticles. Mohammad *et al.*[37] used the ZnO:CNT ETL to improve the crystallinity and charge transfer properties in the PSC. Tavakoli *et al.*[38] employed a multilayer graphene interfacial layer to make smooth contact between ZnO and the perovskite layer and improve the thermal stability of PSCs, which realized a maximum PCE of 19.81%. Wang *et al.*[39] have reported the use of MXene-modified SnO_2 ETLs to realize an enhanced PCE of 20.65%.

From a detailed review of the literature, it is evident that MXene/MO is a suitable alternative supplement to include with the HTLs and ETLs to modify the photoactive layer morphology and promote intimate contact between the transport and photoactive layers, boosting perovskite device performance. Herein, we explore the effect of using MXene/ZnO and MXene/Fe_3O_4-embedded ETL perovskite devices for solar cells and X-ray detectors. The resulting solar cells composed of MXene/ZnO and MXene/Fe_3O_4 ETLs achieved PCEs of 13.31%, and 13.79%, respectively, which are superior to devices using pristine and ZnO- and Fe_3O_4-modified ETL outcomes. Moreover, X-ray detectors using MXene/ZnO and MXene/Fe_3O_4 hybrid composite ETL encompassed modules achieved a lower trap density and superior charge carrier transportation capabilities, resulting in high sensitivities of 4.41 and 4.63 mA per Gy per cm^2, respectively. The metallic MXene nanosheets serve as bridges between MO nanocrystals and make connections that allow the flow of swift charge transfer paths. In addition, because of their high mobility and charge carrier density, the charge can easily travel through the MXene nanoflakes, reducing grain boundaries and discontinuities in the film and potentially extending the exciton's lifetime.

2. Experimental details

2.1 Synthesis of nanocomposites

The synthesis procedures for pure MXenes, ZnO, and Fe_3O_4 from MAX phase Ti_3AlC_2, zinc acetate dihydrate ($Zn(O_2CCH_3)_2(H_2O)_2$), and ferrous chloride ($FeCl_3·6H_2O$) are provided in the ESI.† [40,41] One-step *in situ* calcination was used to synthesize MXene/ZnO and MXene/Fe_3O_4 nanocomposites. Briefly, the as-prepared $Ti_3C_2T_x$ MXene and $FeCl_3·6H_2O$ were liquefied using de-ionized (DI) water under magnetic stirring. Then, 2 M of sodium hydroxide (NaOH) was gradually supplemented under the flow of nitrogen gas. The mixed solution was then subjected to hydrothermal kinetics at 80 °C for 5 h with a solution of pH 12. After the solution slowly reached room temperature, the residues were separated and washed several times with ethanol and DI water *via* centrifugation. The final residues were annealed at 200 °C to form the MXene/Fe_3O_4 nanocomposites. Similarly, to form MXene/ZnO nanocomposites, $Zn(O_2CCH_3)_2(H_2O)_2$ and $Ti_3C_2T_x$ were blended in an ethanol solution under constant stirring. Then, the same procedure mentioned previously was employed to mix the NaOH supplementation and hydrothermal kinetics at 80 °C were followed. After final suspension washing with the support of centrifugation, the residues were vacuum annealed at 200 °C to form MXene/ZnO nanocomposites.

2.2 Device fabrications

The patterned ITO glass substrates (2.5 mm × 2.5 mm) were cleaned in an ultrasonic bath with acetone, methanol, and isopropyl alcohol for 5 min before drying under a nitrogen stream and then dehydrated in a vacuum oven at 100 °C for 10 min. Next, the pre-cleaned ITO glass substrates were subjected to ultraviolet (UV) ozone treatment for 15 min. For the HTL, a poly(3,4-ethylenedioxythiophene)-poly(styrenesulfonate) (PEDOT:PSS) aqueous solution was initially filtered through a 0.45 μm filter and then spin-casted onto an ITO substrate at 3000 rpm for 30 s, followed by annealing at 150 °C for 30 min, affording a thin HTL layer of approximately 40 nm, which was measured by the alpha-step acquisition method. For the perovskite active layer, a perovskite precursor solution containing 25.98 mg of cesium iodide (CsI), 143.1 mg of methylammonium iodide (MAI), and 461 mg of Lead iodide (PbI_2) in a blended solvent of γ-butyrolactone (GBL) : dimethyl sulfoxide (DMSO) (7 : 3, v/v) was prepared and stirred at 60 °C for 12 h. Deposition of the perovskite layer was conducted using a two-step spin coating process: spin casting at 1000 rpm for 10 s followed by spin casting at 3500 rpm for 50 s. During the second step, 300 μL of chlorobenzene was poured onto the perovskite film for 40 s. Then, the deposited film was immediately transferred onto a hot plate and heated at 100 °C for 30 min. The resulting perovskite film thickness was approximately 201 nm. For the ETLs, pure PCBM ETL and nanostructures such as ZnO, Fe_3O_4, MXenes, MXene@ZnO, or MXene@Fe_3O_4-modified ETLs were prepared on the perovskite layer by spin-coating at 1100 rpm for 30 s, followed by annealing at 150 °C for 15 min. Different weight percentages (1, 1.5, 2, and 2.5 wt%) of nanostructures were then blended with PCBM (20 mg mL^{-1}) liquids to form the distinct ETLs. The equipped doped PCBM ETL layer thickness (with and without nanostructures) was approximately 92 nm. Furthermore, LiF (5 nm) and Al (120 nm) films were thermally deposited onto the PCBM ETLs in a vacuum chamber (10^{-6} Torr). Finally, the fabricated devices were encapsulated with UV-curable epoxy glue and a coverslip. The device fabrication process was entirely carried out within the glove box. The assembled devices were taken out after the encapsulation for device characterizations. The ESI† contains all relevant characterization techniques and device experiments.

3. Results and discussion

3.1 Structural properties

Initially, hydrofluoric acid was used to form $Ti_3C_2T_x$ MXenes from the Ti_3AlC_2 MAX phase, which is elaborated upon in the ESI details.† Fig. 1 illustrates the MXene/ZnO and MXene/Fe_3O_4 nanocomposite formation *via* a simple hydrothermal reaction. To verify the configuration of the developed nanostructures, X-ray diffraction (XRD) analyses were conducted on the prepared samples. Fig. S1† presents the XRD pattern of pure MXene sheets, which explores the (002), (006), (008), (0010), (0012) and (110) lattices.[42,43] Fig. 2a illustrates the XRD profiles of the MXene/ZnO and MXene/Fe_3O_4 nanocomposites. The observed XRD directions are well indexed with the standard profiles (JCPDS: 89-6466 (Fe_3O_4) and 80-0074 (ZnO)). For the MXene/Fe_3O_4 composites, the Fe_3O_4 orthorhombic orientations (020), (021), (022), (023), (111), (122), (142), (006), (026), and (154) are exhibited along with a (002) MXene direction (indicated in green). For the MXene/ZnO composites, the hexagonal ZnO (100), (002), (101), (102), (110), (103), and (200) lattices are exhibited along with a (002) MXene direction. These observed structural results strongly evidence the formation of MXene/MO nanocomposites.

To ascertain the functional characteristics of the MXene/MO nanocomposites, Raman scattering analyses were performed on the prepared samples. Fig. 2b displays the Raman spectra of the MXene/ZnO and MXene/Fe_3O_4 nanocomposites. The characteristic MXene peaks explored at 204, 392, 619, and 722 cm^{-1} correlate with the results previously reported in the literature.[42,44] Moreover, the Fe_3O_4 characteristic bands explore the A_{1g} (220 cm^{-1}), T_{2g} (593 and 494 cm^{-1}) and E_g (395 and 281 cm^{-1}) phonon modes to reveal a strong Fe–O relationship in the MXene/Fe_3O_4 composites.[45,46] The high-wavenumber Raman shift realized distinct Fe oxidation, as reported earlier.[47,48] For the pure ZnO nanostructures, a dominant active mode at approximately 439 (E_{2H}) was observed, due to the composing element of the wurtzite structure ZnO with good crystal quality.[49,50] The peaks at approximately 336 and 586 cm^{-1} could be assigned to the Raman A_1(TO) and E_1(LO) mode, respectively.[51,52] Moreover, two wide peaks were evident between 1100 and 1700 cm^{-1} due to the presence of disordered carbon (D) and graphitic carbon (G) peaks, which are

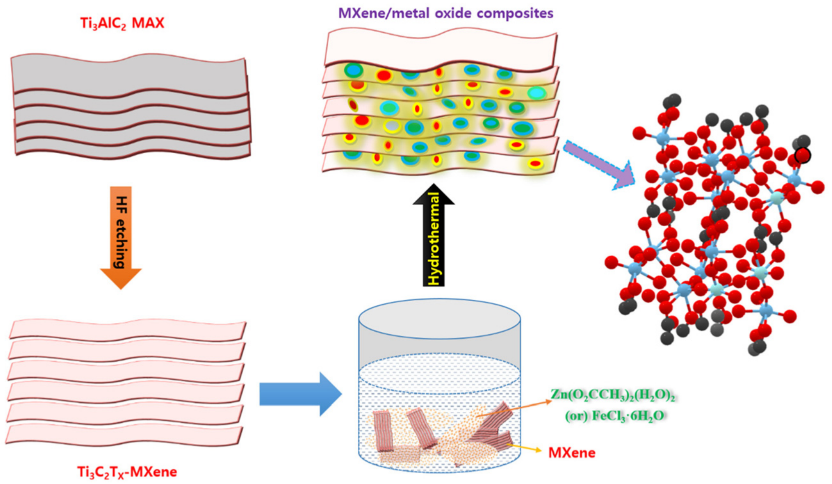

Fig. 1 Schematic for the preparation of metal oxide-interlinked MXene nanocomposites.

credited to the sp^2 sites.[42,53] The exhibited I_D/I_G intensity ratios were 0.78 and 0.99 for MXene/Fe_3O_4 and MXene/ZnO, respectively. The enriched intensity of the G band revealed plentiful graphitic carbon, which can greatly enhance the charge transfer characteristic of the MXene layer, improving the device performance.

X-ray photoelectron spectroscopy (XPS) was performed to assess the elemental composition and oxidation states of the MXene/ZnO and MXene/Fe_3O_4 composites. Fig. 2c–f display the XPS profiles of the Ti 2p, C 1s, Zn 2p, and O 1s regions of the MXene/ZnO nanocomposites, respectively. The Ti 2p region (Fig. 2c) from the MXene/ZnO composite reveals the main characteristic peaks at 454.5 and 463.8 eV due to Ti–C and Ti^{3+}, respectively, along with the representative Ti–O bonding peaks (458.7 and 460.6 eV).[54] Moreover, the C 1s spectrum (Fig. 2d) of the MXene/ZnO composite establishes the Ti–C, C–C and C=O peaks at 281.5, 284.5, and 288.7 eV, respectively. Fig. 2e defines the Zn 2p region of the MXene/ZnO nanocomposites, which establishes twins at 1021.75 and 1044.15 eV due to Zn $2p_{3/2}$ and $2p_{1/2}$, respectively. The observed oxidation state confirmed the existence of a Zn^{2+} valence band, which formed ZnO in the MXene/ZnO composites. For the O 1s region (Fig. 2f), the peaks at 532.1 and 531.4 eV contributed to the Zn–O and C–OH binding energies, respectively. For MXene/Fe_3O_4, the Ti 2p region (Fig. 2g) explores the Ti–C, Ti–O, and Ti^{3+} related peaks at 454.5, 459.9, and 463.3 eV, respectively. The C 1s region (Fig. 2h) gains the Ti–C, C–C, and C=O binding energy peaks from the MXene of the MXene/Fe_3O_4 composites. Fig. 2i defines the Fe 2p binding energy region from the XPS profile, which confirmed the existence of Fe^{3+}- and Fe^{2+}-related $2p_{1/2}$ and $2p_{3/2}$ states along with the Fe satellite peak.[43] The perceived outcomes strongly prove the existence of the multivalent state of Fe and bonding with MXene and O atoms in the composite structure.[55,56] The O 1s deconvoluted profile explores at 529.3, 531.4, and 532.2 eV, which is allotted to C=O, O–C–O, and Fe–O, respectively, as displayed in Fig. 2j.[56] Fig. S2† displays XPS survey profiles of the MXene/ZnO and MXene/Fe_3O_4 composites.

The surface morphologies of the MXene/ZnO and MXene/Fe_3O_4 nanocomposites were characterized by field emission scanning electron microscopy (FESEM) and high-resolution transmission electron microscopy (HRTEM). Fig. 3a–c display the FESEM images of the MXene/ZnO nanocomposites. The magnified images clearly demonstrate the decorated ZnO nanoparticles between the MXene nanosheets (Fig. 3(a and b). The insertion of nanoparticles fills the geometrical defects and creates smooth surface properties for the resulting devices. Moreover, high-resolution images demonstrate the interconnected ZnO nanostructures with uneven grain shapes due to the limited intersection between the nanoparticles. Elemental composition analyses of the prepared MXene/ZnO nanocomposites were also performed. Fig. S3a† displays the energy-dispersive spectral (EDS) profile of the MXene/ZnO composites. The observed results explore the 20, 12, 27, and 41 atomic percentages (at.%) of individual elements O, Zn, C, and Ti, respectively, in the MXene/ZnO composites (Fig. S3b†). Moreover, elemental mapping analyses were performed to visualize the dispersal of elements on the MXene/ZnO composite surface. Fig. S3c–g† clearly depict the identical dispersal of all the elements on the surface of the MXene/ZnO composites, while Fig. 3d displays the formation of arrangements of nanoparticles. The high-resolution images clearly depict defined ZnO nanograin intersections between the MXene sheets. Fig. 3f represents the protruding of ZnO structures on the MXene sheets. In addition, clear lattice fringes with distinct lattice directions (lattice planes are indicated with orange, yellow and white) of the array structure are visible in the high-resolution TEM image (Fig. 3g). Fig. 3h portrays the interfacing atomic arrangements with clear lattice fringes (lattice planes are indicated in yellow and red), while Fig. 3i displays the fast Fourier transform (FFT) pattern, which contains the crystalline pattern of Moire fringes.

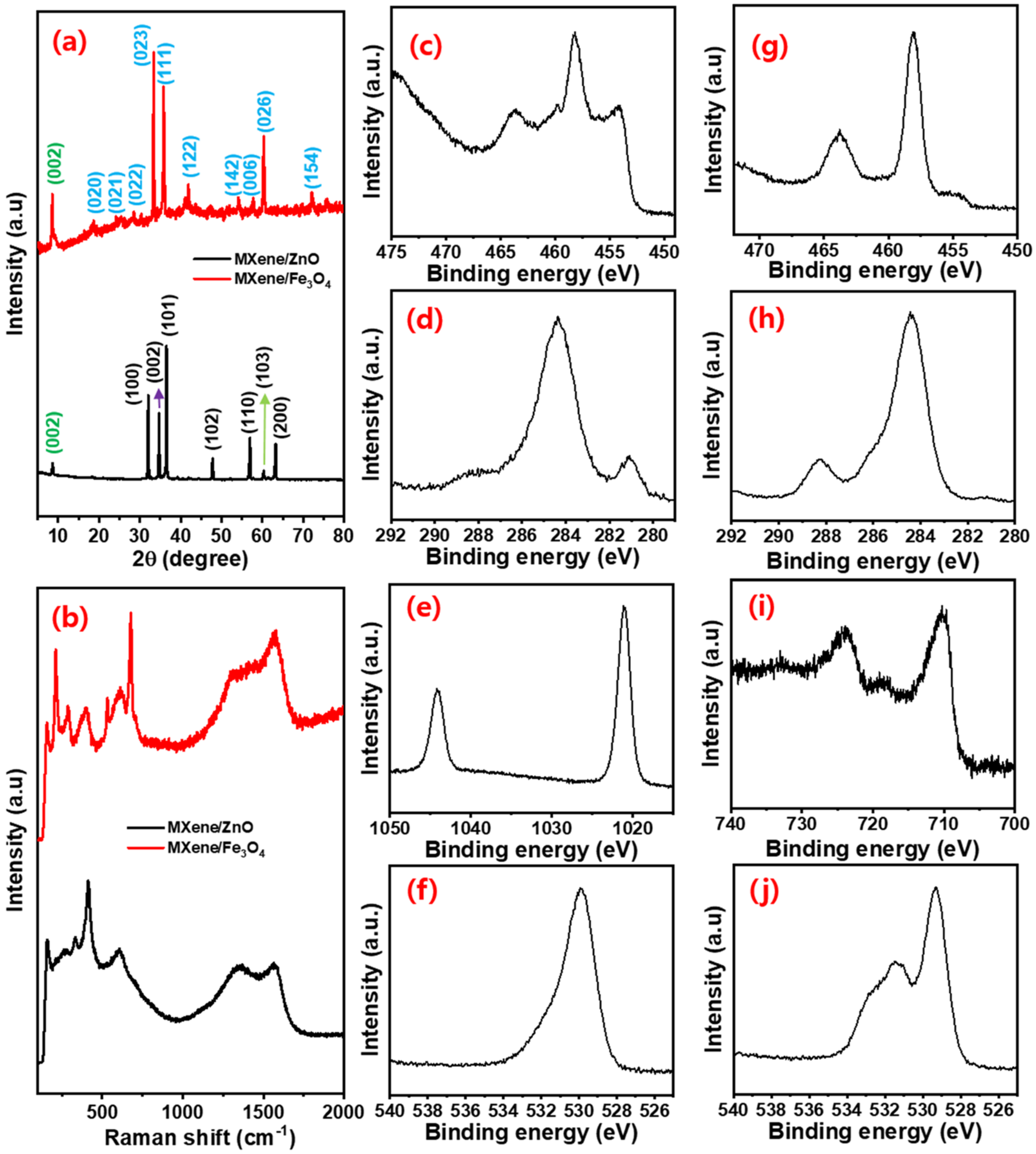

Fig. 2 (a) XRD and (b) Raman profiles of MXene/ZnO and MXene/Fe_3O_4 hybrid nanocomposites. High-resolution XPS spectra: (c) Ti 2p, (d) C 1s, (e) Zn 2p and (f) O 1s for MXene/ZnO nanocomposites; (g) Ti 2p, (h) C 1s, (i) Fe 2p and (j) O 1s for MXene/Fe_3O_4 nanocomposites.

Fig. 4a–c display the FESEM images of the MXene/Fe_3O_4 nanocomposites. The magnified image (Fig. 4a) depicts the decorated Fe_3O_4 nanoparticles between the MXene nanosheets and the edges of the sheets. The covering of Fe_3O_4 nanoparticles on the MXene sheets provides a protective layer, allowing the development of strong geometrical interactions and enriched surface properties. Moreover, the high-resolution image (Fig. 4c) demonstrates the strongly adhered MO particles between the MXenes. Fig. S4a† displays the EDS profile of the MXene/Fe_3O_4 composites. The observed results explore 24, 15, 23, and 38 at% of the individual elements O, Fe, C, and Ti, respectively, in the MXene/Fe_3O_4 composites (Fig. S4b†). Fig. S4c† confirms the elemental distribution of all the elements on the MXene/Fe_3O_4 composites. Fig. S4d–g† clearly depict the constant dispersal of Fe, O, Ti, and C elements, respectively, on the surface of MXene/Fe_3O_4 composites, while Fig. 4d depicts the development of nanosized grains. The high-resolution images (Fig. 4e and f) clearly display the different sizes of Fe_3O_4 nanograin intersections along the MXene sheets (lattice planes are indicated in different colors). Fig. 4g displays the high-resolution TEM image that indicates obvious lattice fringes with unified lattice directions (highlight with different color) along the array structure. In addition, defined atomic arrangements and lattice intersections with selective defective characteristics can be detected in the high-resolution TEM micrograph (Fig. 4h). Fig. 4i presents the FFT pattern, which contains a well-organized pattern of Moire fringes that represent the high-quality crystalline behavior of the prepared MXene/Fe_3O_4 nanocomposites.

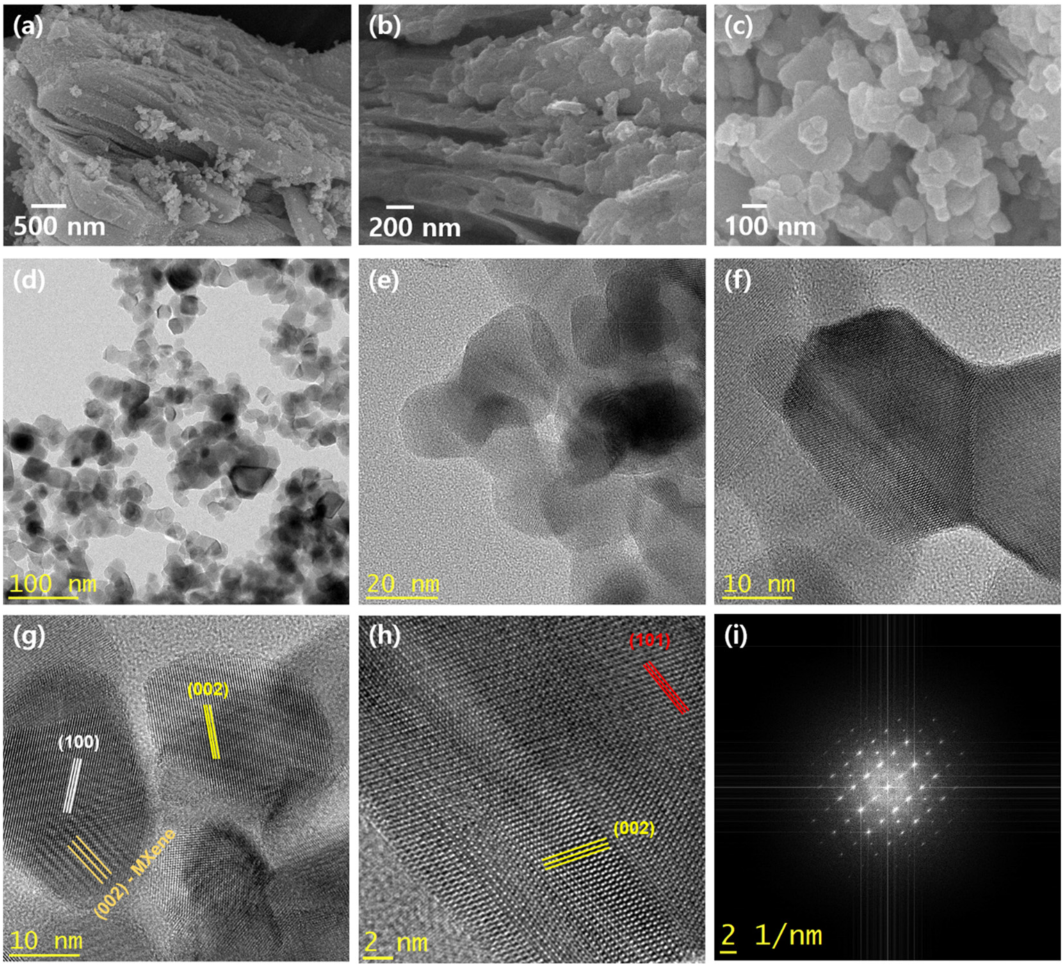

Fig. 3 Microscopic studies of MXene/ZnO nanocomposites: (a–c) different magnifications of FESEM images; (d) low-resolution HRTEM micrograph; (e and f) high-resolution HRTEM with interfaced hexagonal grains; (g) lattice fringes on high-resolution HRTEM; (h) atom arrangements of mixed-phase MXene/ZnO nanocomposites; and (i) FFT pattern.

3.2 Perovskite solar cells

In this section, we explore the influence of metal oxides and MXenes (and their nanocomposites) on the photovoltaic performance of perovskite-based solar cells. For this work, we employed a highly active cesium-encompassed methyl ammonium lead iodide ($Cs_{0.1}MA_{0.9}PbI_3$) matrix as a perovskite active layer to achieve enhanced device performance. To conduct a detailed investigation, pure Fe_3O_4, ZnO, and MXenes were employed as doping materials, the PCBM and FESEM images of which are provided in Fig. S5–S7 in the ESI,† respectively. Usually, the PCBM layer is used as an ETL in perovskite structures. However, in this work, we adjusted the PCBM ETL by amalgamating with ZnO, Fe_3O_4, MXene, MXene/ZnO, and MXene/Fe_3O_4 nanostructures. Fig. 5a presents the schematic of the prepared module of the device using a nanocomposite-doped ETL layer with a prototype of ITO/PEDOT:PSS/$Cs_{0.1}MA_{0.9}PbI_3$/nanostructures@PCBM/LiF/Al. Fig. 5b displays the cross-sectional FESEM image of the prepared device structure with a MXene/MO using the modulated PCBM ETL. The structure of the prepared device confirmed a layered architecture. Tauc plots were constructed to analyse the optical bandgap of the prepared nanostructures using the UV-vis absorption profiles.[57–59] Fig. S8a–d† shows the optical band position of Fe_3O_4, ZnO, MXene/Fe_3O_4 and MXene/ZnO nanostructures, respectively. The plotted results are explored the 2.4 eV, 3.3 eV, 2.6 eV and 1.9 eV optical band gap for the pure Fe_3O_4, pure ZnO, MXene/Fe_3O_4 and MXene/ZnO nanostructures, respectively. Fig. S9a and b† shows the ultraviolet photoelectron spectral (UPS) results for the ZnO- and Fe_3O_4-based nanostructures, respectively. From the UPS result, the conduction band minimum (CBM) level can be obtained as described in the equation, $E_{\mathrm{CBM}} = 21.2 - (E_{\text{cut-off}} - E_{\mathrm{Fermi}})$.[60,61] $E_{\text{cut-off}}$ can be extracted from the defined position as shown in Fig. S9c and d† for the ZnO- and Fe_3O_4-based nanostructures, respectively. However, the Fermi energy position ($\mathrm{E}_{\mathrm{Fermi}}$) can be derived from the Fermi region as defined in Fig. S9e and f,† respectively. Finally, the valence band maximum (VBM) was estimated after the deduction of optical band gap from the CBM position. Fig. 5c and d display the energy level band

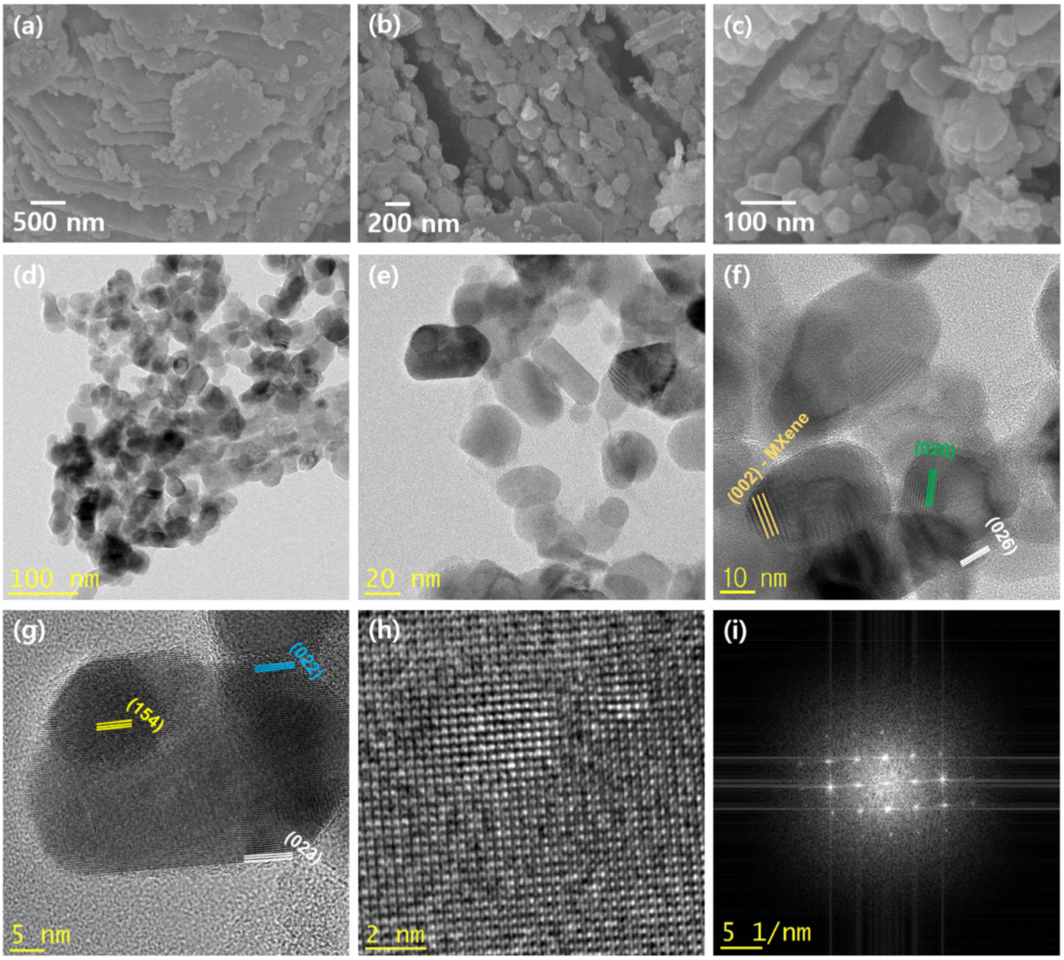

Fig. 4 Microscopic studies of MXene/Fe_3O_4 nanocomposites: (a–c) different magnification of FESEM images; (d) low-resolution HRTEM micrograph; (e and f) high-resolution HRTEM with cuboidal and ellipsoidal shaped grains; (g) selected region lattice fringes of high-resolution HRTEM images; (h) atom interaction and arrangements of mixed-phase MXene/Fe_3O_4 nanocomposites; and (i) FFT pattern.

alignment of the PCBM ETL–blended devices that incorporate MXene/Fe_3O_4 and MXene/ZnO nanocomposites, respectively. The inclusion of nanocomposites with the PCBM provides more favorable VBM and CBM positions to realize a feasible electron flow to attain the electrode.[62,63] Furthermore, to realize the work function variation for the pure ZnO and Fe_3O_4 nanostructure-modulated energy level, the band alignments are demonstrated in Fig. S10a and b,† respectively. When electrons are transferred from the active layer to the cathode *via* the ETL, the MXene/MO-modulated PCBM acts as a bridge, where the doped MXene/MO nanocomposites substantially decrease the energy difference between the VBM and CBM during charge separations at the perovskite/ETL junction. In summary, the charge extraction or dissociation and transfer of free charge carriers (or excitons) in the prepared perovskite devices with MXene/MO-modulated PCBM are fast, and the rate of recombination is expected to be low, establishing superior device characteristics.

To prepare the device prototypes, the current-density voltage (*J*–*V*) characteristics were detected at 100 mW cm^{-2} under AM 1.5G solar radiance for the pure PCBM ETL and different nanostructures (MXene, ZnO, Fe_3O_4, MXene/ZnO, and MXene/Fe_3O_4) using modulated PCBM ETL–encompassed solar cells. Different weight percentages of the nanostructures (1, 1.5, 2, and 2.5 wt%) were doped with PCBM to form effective ETLs and their properties were assessed. Fig. 6a displays the *J*–*V* curves of constructed devices with pure PCBM and 2 wt% MXene, ZnO, Fe_3O_4, MXene/ZnO, and MXene/Fe_3O_4 using modulated PCBM ETL-encompassed perovskite solar cells. A prepared device using a $Cs_{0.1}MA_{0.9}PbI_3$ active layer with a pure PCBM ETL produced an excellent open circuit voltage (V_{OC}) and short-circuit current density (J_{SC}) of 0.895 V and 20.5 mA cm^{-2}, respectively. Moreover, the prepared device explores 10.58% of PCE along with 57.6% of fill factor (FF), which were higher than those of the device composed of a pure $MAPbI_3$ active layer (8.92%), as reported previously.[4] When devices were prepared with different amounts of ZnO (1–2.5 wt%) using the modulated PCBM ETL, the *J*–*V* characteristics fluctuated surprisingly based on the amount of doping ZnO nanostructures. Fig. S11† displays the *J*–*V* characteristics

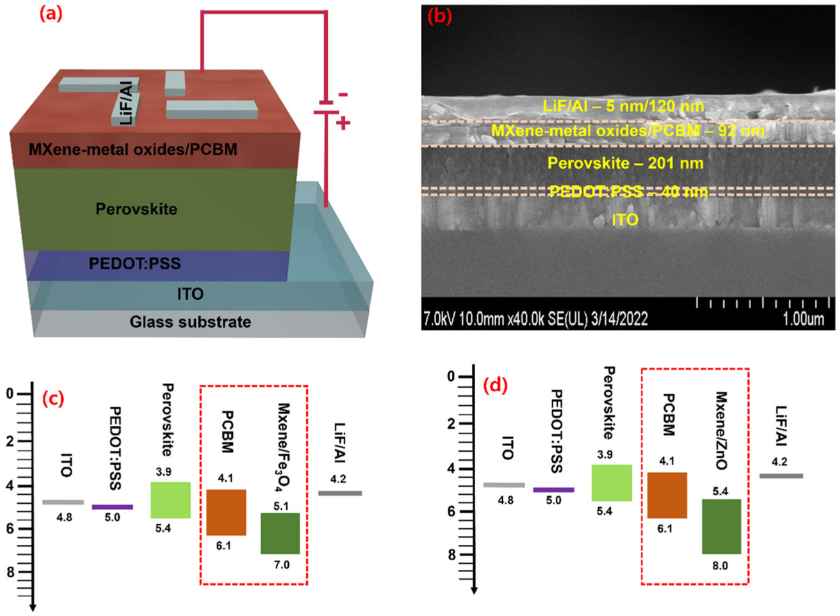

Fig. 5 (a) Schematic of the assembled device; (b) cross-sectional FESEM image of the prepared device; energy level of (c) ITO/PEDOT:PSS/$Cs_{0.1}MA_{0.9}PbI_3$/MXene-Fe_3O_4@PCBM/LiF/Al and (d) ITO/PEDOT:PSS/$Cs_{0.1}MA_{0.9}PbI_3$/MXene-ZnO@PCBM/LiF/Al.

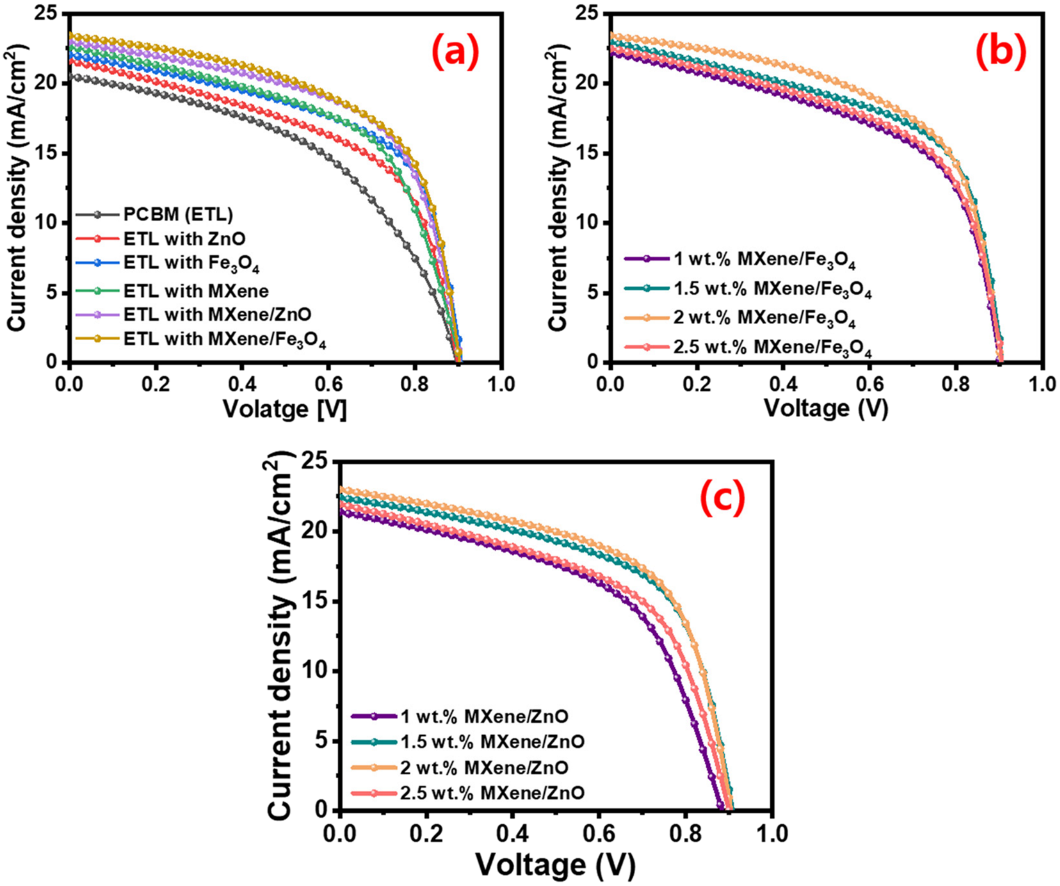

Fig. 6 (a) *J*–*V* profiles of pure PCBM and optimized 2% of ZnO, Fe_3O_4, MXene, MXene/ZnO, and MXene/Fe_3O_4-doped ETL-comprised solar cells; *J*–*V* curves of 1, 1.5, 2, and 2.5% of (b) MXene@Fe_3O_4 and (c) MXene@ZnO-doped ETL-comprised solar cells.

of perovskite solar cells with 1, 1.5, 2, and 2.5 wt% of ZnO-doped PCBM ETL. Here, including ZnO with PCBM ETL produced significant improvements in the device performance, as demonstrated in Table S1.† The PCE of the constructed devices significantly improved to 10.31%, 11.23%, and 11.67% for 1, 1.5, and 2 wt% of ZnO-doped PCBM ETL devices, respectively. However, a device realizes the decrement of PCE beyond 2 wt% of ZnO doping with the PCBM ETL, whereas the PCE reduced to 10.88% for the prepared device with 2.5 wt% of ZnO-doped PCBM ETL.

The *J*–*V* characteristics were modulated based on the amount of MXenes doped with the PCBM ETL, and the results are provided in Fig. S12.† As expected, including MXenes with the PCBM ETL enriched device performances significantly, as demonstrated in Table S2.† When the PCBM was doped with 1 wt% of MXenes to make the ETL, the resulting device achieved a PCE of 11.21%. Moreover, devices incorporating 1.5 and 2 wt% of MXene-modulated PCBM ETL realized PCEs of 12.12% and 12.84%, respectively, whereas the device with 2.5 wt% of MXene-doped PCBM ETL achieved a low PCE of 11.73%. This could be due to the high amount of doping altering the core of the PCBM matrix. Fig. S13† displays the *J*–*V* profiles of modulated PCBM ETL devices composed of different amounts of Fe_3O_4. The prepared devices exhibit PCEs of 10.81%, 11.78%, 12.23%, and 11.26% for devices constructed with 1, 1.5, 2 and 2.5 wt% of Fe_3O_4-doped PCBM ETL (Table S3†). The observed results with Fe_3O_4-modulated ETL give a similar trend of device performance, as discussed previously.

To reveal the effect of the amalgamated matrix on ETL fabrication, MXene/Fe_3O_4 and MXene/ZnO nanocomposites were introduced with different doping percentages, and the results are provided in Fig. 6b and c, respectively. Table S4† elaborates on the perovskite solar cell parameters with different amounts of MXene/Fe_3O_4-modulated ETLs. A device composed of 1 wt% of MXene/Fe_3O_4 using modulated ETL realized improved *J*–*V* characteristics. The estimated parameters were V_{OC} = 0.901 V, J_{SC} = 22.2 mA cm^{-2}, PCE = 12.24%, and FF = 61.2%. When the doping content of MXene/Fe_3O_4 was increased to 1.5 wt% in the ETL, the following were observed for the prepared device: V_{OC} = 0.906 V, J_{SC} = 22.9 mA cm^{-2}, PCE = 13.25%, and FF = 63.7%. Superior device performance was achieved for 2 wt% of MXene/Fe_3O_4 using the modulated ETL-incorporated perovskite solar cell device with a maximum PCE of 13.79% and V_{OC} = 0.902 V, J_{SC} = 23.4 mA cm^{-2}, and FF = 65.2% of. Further, 2.5 wt% of MXene/Fe_3O_4-modified ETL achieved a PCE of 12.76%. Table S5† elaborates on the perovskite solar cell parameters with different amounts of MXene/ZnO-modulated ETLs. When 1 wt% of MXene/ZnO was used to modulate the ETL, the prepared device achieved a V_{OC} of 0.884 V, a J_{SC} of 21.4 mA cm^{-2}, a PCE of 11.86%, and an FF of 62.7%. Further, 1.5 wt% MXene/ZnO in the ETL created a PCE of 12.82% with a V_{OC} of 0.908 V, a J_{SC} of 22.4 mA cm^{-2}, and an FF of 62.9%. A maximum PCE of 13.31% was realized for 2 wt% of MXene/ZnO using the modulated ETL-incorporated perovskite solar cell device in addition to a V_{OC} of 0.904 V, a J_{SC} of 22.9 mA cm^{-2}, and an FF of 64.1%. Further, 2.5 wt% of MXene/ZnO-modified ETL achieved a PCE of 12.34%. These *J*–*V* characteristics clearly proved that 2 wt% doping of nanostructures produced efficient variations in the device performance. The observed device characteristics for pure PCBM and 2 wt% MXene, ZnO, Fe_3O_4, MXene/ZnO, and MXene/Fe_3O_4 using modulated PCBM ETL are provided in Table 1.

Table 1 Photovoltaic performance of the prepared perovskite devices with pure and 2 wt% MXene, ZnO, Fe_3O_4, MXene/ZnO, and MXene/Fe_3O_4 composite-blended ETLs

Device	V_{OC} [V]	J_{SC} [mA cm^{-2}]	FF [%]	PCE [%]	R_S [Ω cm^2]
PCBM (ETL)	0.895	20.512	57.63	10.58	169.31
ETL with ZnO	0.897	21.623	60.16	11.67	158.42
ETL with Fe_3O_4	0.907	22.037	61.18	12.23	150.17
ETL with MXene	0.905	22.598	62.78	12.84	143.18
ETL with Mxene@ZnO	0.904	22.987	64.05	13.31	138.76
ETL with Mxene@Fe_3O_4	0.902	23.421	65.27	13.79	132.65

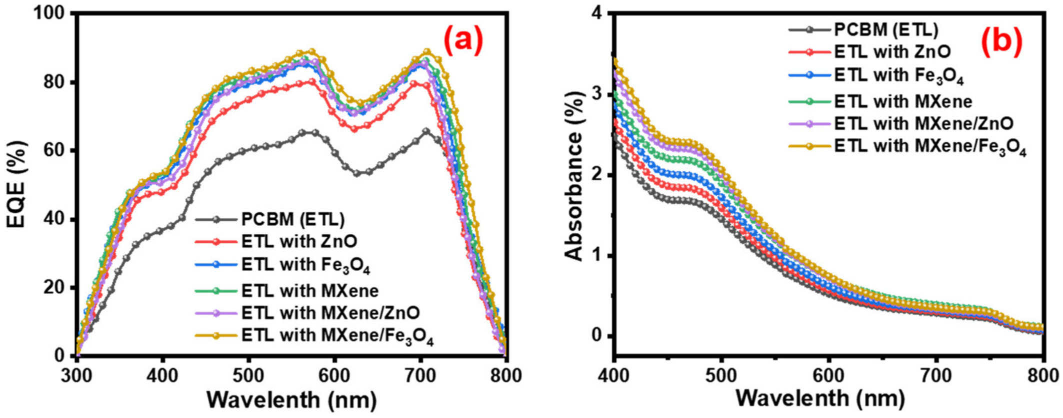

Fig. 7 (a) EQE of assembled device using pure and 2 wt% of ZnO, Fe_3O_4, MXene, MXene/ZnO, and MXene/Fe_3O_4-doped ETLs. (b) Absorption lines for pure and 2 wt% of ZnO, Fe_3O_4, MXene, MXene/ZnO, and MXene/Fe_3O_4-doped ETL.

The perceived outcomes determined the maximum responsive characteristics of prepared devices with the 2 wt% of nanostructure-doped ETL. Hence, external quantum efficiency (EQE) measurements were conducted for pure and optimum MXene, ZnO, Fe_3O_4, MXene/ZnO, and MXene/Fe_3O_4 nanostructures using modulated PCBM ETL-composed solar cells, as displayed in Fig. 7a. The EQE measurements were conducted between wavelengths of 300 and 800 nm. A device composed of pure PCBM ETLs produces approximately 60% of the EQE curve in the visible region of wavelengths owing to their intrinsic characteristics.[64] Further, the EQE profile evidently increased for the 2 wt% of nanostructure-doped ETL-composed devices. A trend of EQE profile suddenly increasing was observed (from a null to 88%) between the 300 and 600 nm wavelengths for the 2 wt% MXene/Fe_3O_4-doped PCBM ETL-incorporated device. In addition, the EQE declined slightly at the end of the visible region and increased significantly again at the near-IR region. A similar trend was observed for different ETL-composed devices, which could be caused by the interaction barrier between the active and transport layers during the charge carrier transport. The visible region of the EQE spectra enhancement could also be attributed to the enhanced J_{SC} of the resulting devices.[65] The establishment of an enriched photocurrent was primarily attributed to the enhanced charge carriers' mobility (to some degree), rather than the altered light collecting properties of the devices.[66]

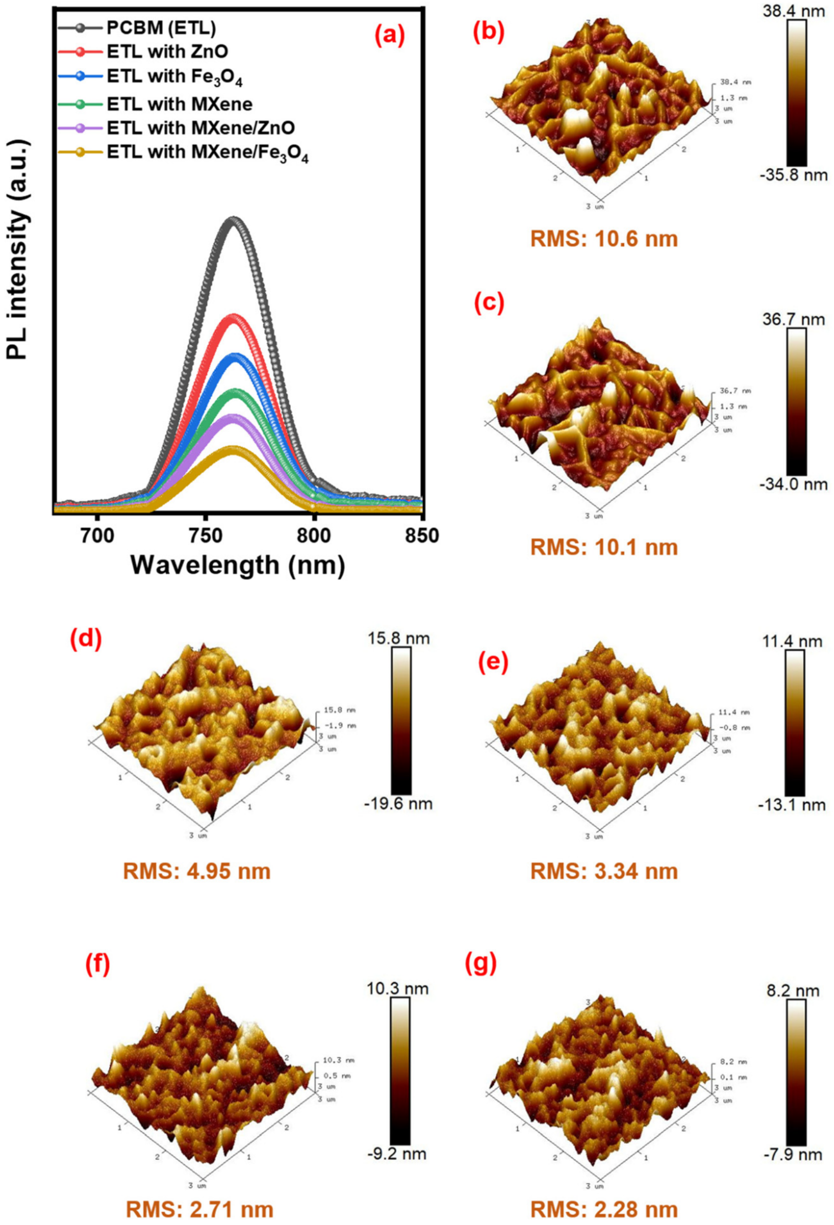

Fig. 8 (a) Photoluminescence spectra of PCBM and 2 wt% of ZnO, Fe_3O_4, MXene, MXene/ZnO, and MXene/Fe_3O_4-doped PCBM onto ITO. AFM image of (b) pure PCBM and 2 wt% of (c) ZnO, (d) Fe_3O_4, (e) MXene, (f) MXene/ZnO, and (g) MXene/Fe_3O_4-doped PCBM onto ITO.

Fig. 7b presents the UV-Vis-NIR absorption outlines of pure and 2 wt% MXene, ZnO, Fe_3O_4, MXene/ZnO, and MXene/Fe_3O_4 using modulated PCBM ETLs. The observations realized the considerable improvement of absorption characteristics due to the 2 wt% of nanostructures doping with PCBM ETL which authorized the enhanced light reaping characteristics of doped ETLs. These characteristics emanate from the improved surface interactions between the active layer and the ETL.

To reveal the origin of device performance, we investigated the charge transportation characteristics using PL studies for PCBM (ETL) and their hybridization with ZnO, Fe_3O_4, MXene, MXene/ZnO, and MXene/Fe_3O_4 onto ITO (Fig. 8a). All these layers exhibited a clear PL peak at 760 nm, which resulted from $MAPbI_3$.[67] The results indicated that the quantum yield of perovskite PL was significantly reduced for hybrid composites that included the PCBM ETL. This could be due to the inhibition of electron–hole pair recombination processes caused by PL quenching related to the increased performance of photoconversion. It was revealed that PL quenching efficiency was in the following order: PCBM (ETL) < ETL with ZnO < ETL with Fe_3O_4 < ETL with MXene < ETL with MXene/ZnO < ETL with MXene/Fe_3O_4. Atomic force microscopic (AFM) measurements were conducted to study the topographical properties of nanostructure-doped ETLs (Fig. 8b–g). The topologies of the prepared PCBM layers clearly exhibit peculiar alterations due to the doping of different nanostructures. The observed surface roughness was approximately 10.6, 10.1, 4.95, 3.34, 2.71, and 2.28 nm for the pure and MXene, ZnO, Fe_3O_4, MXene/ZnO, and MXene/Fe_3O_4-doped ETLs, respectively. The diminished surface roughness for the nanostructure-blended ETLs strongly suggests strong interfacial characteristics with the perovskite active layer and electrode, thereby achieving high device performances. Furthermore, the incorporated nanostructures could fill the voids and defective areas of the PCBM matrix, thereby offering compact surface characteristics for ETL formation and allowing many photo-generated carriers through the ETL for enhanced recombination properties.[68] The comparable PCE improvements as elaborated in Table S6† with various literature studies strongly ascertained the improved device characteristics due to the inclusion of MXene/Fe_3O_4 and MXene/ZnO-modified ETLs.

3.3 X-ray detectors

To demonstrate the photodetector response characteristics of the perovskite-based devices, the fabricated module was connected to a scintillator for X-ray detection.[69] To appraise the photoreactivity, four-cell devices were developed using the pure and optimum (2 wt%) MXene, ZnO, Fe_3O_4, MXene/ZnO, and MXene/Fe_3O_4-modulated PCBM ETLs (ITO/PEDOT: PSS/$Cs_{0.1}MA_{0.9}PbI_3$/nanostructures@PCBM/LiF/Al). Fig. 9a displays the layout of prepared photodetectors with the stacking of PEDOT:PSS HTL, $Cs_{0.1}MA_{0.9}PbI_3$ active layer, and nanostructure (MXene, ZnO, Fe_3O_4, MXene@ZnO, and MXene@Fe_3O_4) – modified ETL and cathode on a patterned ITO substrate. Fig. 9b validates the log J–V lines of the perovskite-based X-ray detectors with pure and optimized MXene, ZnO, Fe_3O_4, Mxene/ZnO, and MXene/Fe_3O_4-doped PCBM ETL

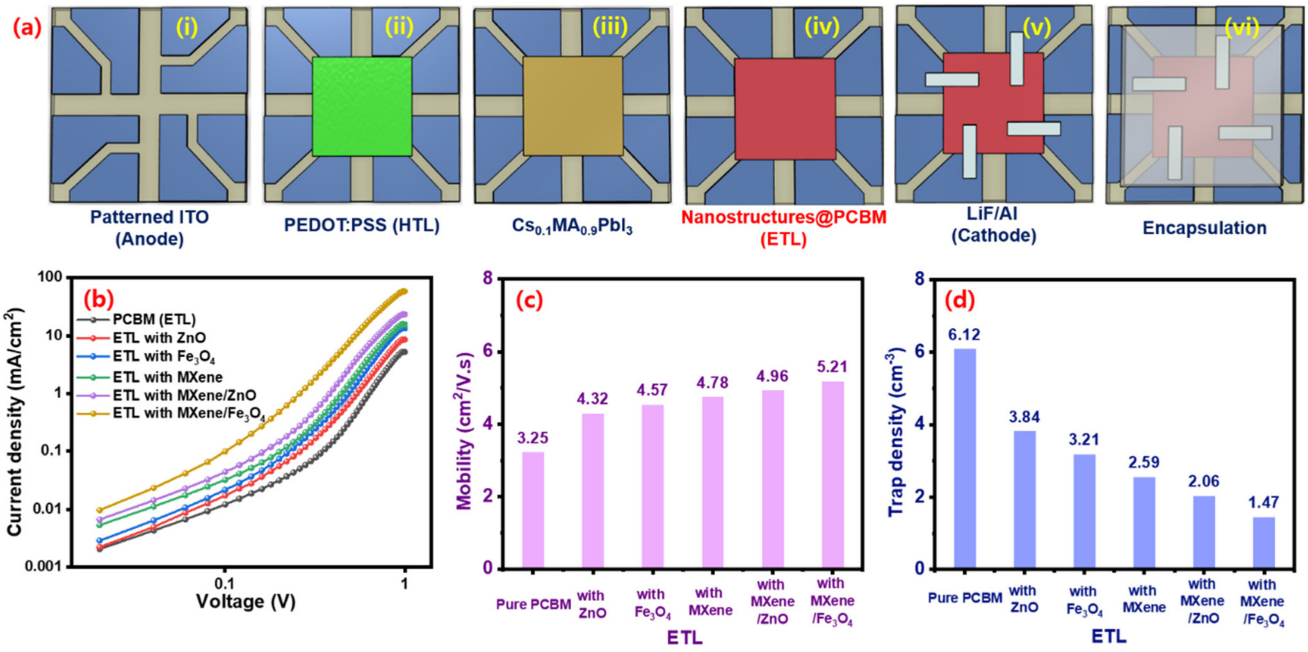

Fig. 9 (a) Step-by-step fabrication of X-ray detectors using nanostructure-doped PCBM ETL: (i) patterned ITO/glass, (ii) ITO/PEDOT:PSS, (iii) ITO/HTL/$Cs_{0.1}MA_{0.9}PbI_3$, (iv) ITO/HTL/$Cs_{0.1}MA_{0.9}PbI_3$/nanostructures@PCBM, (v) ITO/HTL/$Cs_{0.1}MA_{0.9}PbI_3$/nanostructures@PCBM/LiF/Al and (vi) encapsulation. (b) log J–V profiles and (c) mobility. (d) Trap density variations for the pure and 2% of MXene, ZnO, Fe_3O_4, MXene/ZnO, and MXene/Fe_3O_4 nanostructure-doped PCBM ETL-involved X-ray detectors.

devices. The Mott–Gurney relationship was used to determine charge carrier mobilities using the log$J$–V relations:[70]

$$J = \frac{9}{8}\varepsilon_r\varepsilon_0\mu\frac{V^2}{L^3}. \tag{1}$$

where μ is the carrier mobility, ε_r the active layer relative dielectric constant, V the voltage applied to the appliance, ε_0 the free space permittivity (8.85×10^{-12} F m^{-1}), and L the active layer thickness. Fig. 9c displays the mobility variations for the different ETL-composed devices. The acquired mobilities were at 3.25×10^{-4}, 4.78×10^{-4}, 4.32×10^{-4}, 4.57×10^{-4}, 4.96×10^{-4}, and 5.21×10^{-4} cm^2 V^{-1} s^{-1} for the pure and optimum MXene, ZnO, Fe_3O_4, MXene/ZnO, and MXene/Fe_3O_4 nanostructure-blended PCBM ETLs, respectively. The swift mobility explores the X-ray detector with the MXene/Fe_3O_4 nanostructure-blended PCBM ETL. The trap densities (N_t) were calculated from the log$J$–V profile fitted lines as expanded in eqn (2):[19]

$$\text{Trap density}\ (N_t) = \frac{2V_{\text{TFL}}\varepsilon_r\varepsilon_0}{qL^2}, \tag{2}$$

where q denotes the charge and V_{TFL} the onset voltage of the trap-filled limit region. Fig. 9d presents the acquired N_t for the different ETL-composed X-ray detectors. The results were 6.12×10^{15}, 2.59×10^{15}, 3.84×10^{15}, 3.21×10^{15}, 2.06×10^{15}, and 1.47×10^{15} cm^2 V^{-1} s^{-1} for the pure and optimum MXene, ZnO, Fe_3O_4, Mxene/ZnO, and MXene/Fe_3O_4 nanostructure-blended PCBM ETLs, respectively. The low trap densities for the nanocomposite structures further proved the possibility of enriching the photodetection properties.

The photodetection parameters of the CCD–DCD and the detection sensitivities were measured for different ETL-composed devices, as displayed in Table 2. The estimated results explored that the MXene/ZnO and MXene/Fe_3O_4 nanocomposite-blended PCBM ETL-integrated devices achieved high sensitivities of 4.41 and 4.63 mA per Gy per cm^2, respectively. These results are superior to the other ETL-composed devices such as pure PCBM (3.12 mA per Gy per cm^2), MXene@PCBM (4.16 mA per Gy per cm^2), ZnO@PCBM (3.64 mA per Gy per cm^2), and Fe_3O_4@PCBM (3.87 mA per Gy per cm^2). The collected CCD-DCD were at 10.42, 13.89, 12.16, 12.93, 14.73, and 15.46 μA cm^{-2} for the pure and the 2% of MXene, ZnO, Fe_3O_4, MXene/ZnO, and MXene/Fe_3O_4 nanostructure-doped PCBM ETLs, respectively. Moreover, the measured J_{SC} values were 20.5, 22.6, 21.6, 22.0, 22.9, and 23.4 mA cm^{-2}, respectively, for the pure and optimum MXene, ZnO, Fe_3O_4, MXene/ZnO, and MXene/Fe_3O_4-doped PCBM hybrid ETLs, respectively, as illustrated in Table 2. Different concentrations (1, 1.5, 2, and 2.5 wt%) of MXene, ZnO, Fe_3O_4, MXene/ZnO, and MXene/Fe_3O_4 blended with the PCBM ETL comprising the X-ray detector device characteristics are specified in the Tables S7–S11,† respectively. The improvement in device performance was credited to the increased energy level synchronization between PCBM and the nanostructures, which could effectively reorganize the surface regulation, thereby easing swift carrier transport and boosting the charge collection efficiency at the interface.

Table 2 X-ray photodetection properties of the prepared perovskite devices with pure and 2 wt% MXene, ZnO, Fe_3O_4, MXene/ZnO, and MXene/Fe_3O_4 composite-blended ETLs

Device	CCD–DDC [μA cm^{-2}]	Sensitivity [mA per Gy per cm^2]	Conductivity [S cm^{-1}]
PCBM (ETL)	**10.42**	**3.12**	412.23
ETL with ZnO	12.16	3.64	481.78
ETL with Fe_3O_4	12.93	3.87	533.14
ETL with MXene	13.89	4.16	591.57
ETL with Mxene@ZnO	14.73	4.41	612.11
ETL with Mxene@Fe_3O_4	15.46	4.63	632.23

The capability of the prepared highly efficient X-ray detector using the MXene/Fe_3O_4-doped PCBM ETL was analyzed using different operation conditions. To determine the role of the applied X-ray source on device behavior, different applied voltages of −0.2 to −1.0 V were used to analyze device sensitivity and CCD–DCD. Fig. 10a displays the CCD–DCD and detection sensitivity of the MXene/Fe_3O_4-doped PCBM hybrid ETL-composed detector. The linear enhancement observes with the

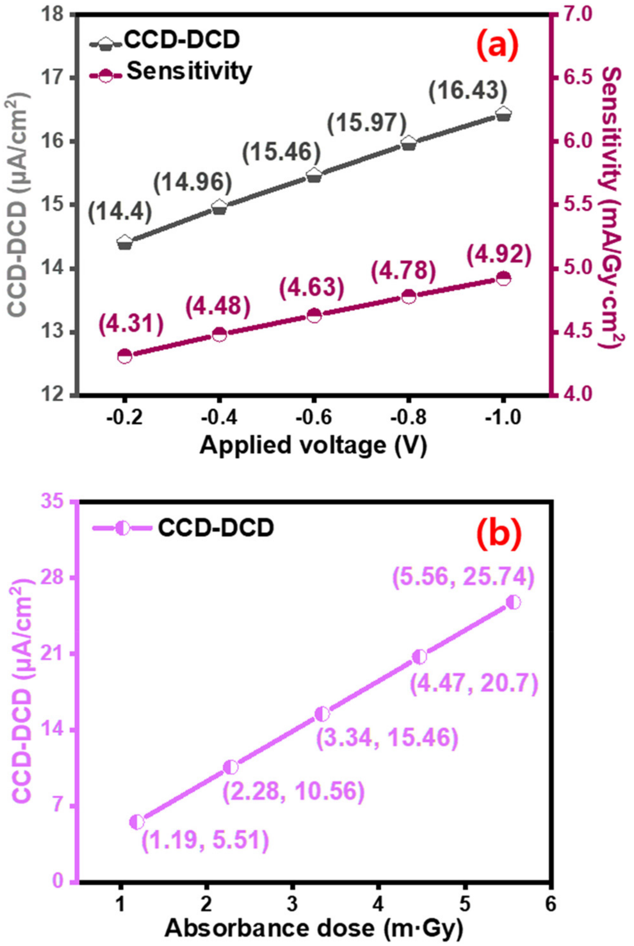

Fig. 10 (a) CCD–DCD and sensitivity at different applied bias voltages. (b) Different dose rate performance of MXene/Fe_3O_4-doped PCBM ETL using the fabricated X-ray detector.

amount of applied voltage for the constructed X-ray detector. A maximum sensitivity of 4.92 mA per Gy per cm^2 was observed with an applied voltage of −1.0 V for the prepared X-ray detector using the MXene/Fe_3O_4-doped PCBM ETL. Moreover, the observed CCD–DCD was between 14.4 and 16.43 μA cm^{-2} at the various applied voltages of the prepared X-ray detector (Fig. 10a, right panel).

In addition, to define the prepared X-ray detector responsivity, different absorbance doses (1.19, 2.28, 3.34, 4.47, and 5.56 m Gy) were incident on the detector to evaluate their capacity. Fig. 10b portrays the CCD–DCD variations in terms of different absorbed X-ray dosages on the MXene/Fe_3O_4-doped PCBM hybrid ETL-composed detector. The results strongly confirmed the enhancement at the rate of absorbance dose for the prepared X-ray detectors. Hence, the nanocomposite-incorporated ETL devices achieved enhanced detection properties, including a superior hybrid interfacial structure, smooth morphology, good energy level alignment with the active layer, and suppressed rate of carrier recombination, which allow for easy electron transportation/extraction and rapid exciton charge dissociation.

4. Conclusion

In this work, we demonstrated MXene, ZnO, and Fe_3O_4 and their hybrid nanocomposite-modified fullerene derivative ETL's role in perovskite-based solar cells and X-ray detector activity. The Raman and XRD results clearly ascertained the formation of MXene/ZnO and MXene/Fe_3O_4 nanocomposites. The derived microscopic results visualized the mixed-phase atom interactions and arrangements on the nanocomposite architecture. Systematic investigations were conducted with different doping wt% inclusion of prepared nanostructures with the PCBM ETL and detailed studies were conducted for the solar cell and X-ray detection. The MO-decorated MXene nanosheets produced low internal interfacial resistance and suppressed oxygen vacancies, making an effective bridge for rapid carrier transference within the assembled devices. The 2 wt% of nanocomposites using a modulated ETL-incorporated perovskite solar cell device exhibited maximum PCEs of 13.79% and 13.31%, respectively. The swift the EQE performance occurred in the visible and NIR regions of the solar cell with the MXene/Fe_3O_4-modulated ETL. Furthermore, MXene/ZnO and MXene/Fe_3O_4 using the assembled X-ray photodetector achieved excellent sensitivities of 4.41 and 4.63 mA per Gy per cm^2, respectively. The influences of different applied voltages and dose rates were strongly affirmed by the assembled X-ray detection characteristics. Hence, the tuning of ETLs with the support of MXene-based nanocomposites would be the novel way of tuning perovskite-based solar cells and photodetector properties for efficient future device fabrication.

Conflicts of interest

There are no conflicts to declare.

Acknowledgements

This work was supported by the Mid-career Researcher Program through the National Research Foundation of Korea (NRF) funded by the Ministry of Science and ICT (No. 2019R1A2C2086747).

References

1 N. J. Jeon, J. H. Noh, W. S. Yang, Y. C. Kim, S. Ryu, J. Seo and S. I. Seok, *Nature*, 2015, **517**, 476–480.
2 H. Zhou, Q. Chen, G. Li, S. Luo, T.-b. Song, H.-S. Duan, Z. Hong, J. You, Y. Liu and Y. Yang, *Science*, 2014, **345**, 542–546.
3 Q. Dong, Y. Fang, Y. Shao, P. Mulligan, J. Qiu, L. Cao and J. Huang, *Science*, 2015, **347**, 967–970.
4 D. Vikraman, H. Liu, S. Hussain, S. H. A. Jaffery, K. Karuppasamy, E.-B. Jo, Z. Abbas, J. Jung, J. Kang and H.-S. Kim, *Small*, 2022, **18**, 2104216.
5 R. He, S. Ren, C. Chen, Z. Yi, Y. Luo, H. Lai, W. Wang, G. Zeng, X. Hao and Y. Wang, *Energy Environ. Sci.*, 2021, **14**, 5723–5759.
6 R. W. Crisp, F. S. Hashemi, J. Alkemade, N. Kirkwood, G. Grimaldi, S. Kinge, L. D. Siebbeles, J. R. van Ommen and A. J. Houtepen, *Adv. Mater. Interfaces*, 2020, **7**, 1901600.
7 R. Turtos, S. Gundacker, S. Omelkov, B. Mahler, A. Khan, J. Saaring, Z. Meng, A. Vasil'ev, C. Dujardin and M. Kirm, *npj 2D Mater. Appl.*, 2019, **3**, 1–10.
8 C. Szeles, *Phys. Status Solidi B*, 2004, **241**, 783–790.
9 S. Shrestha, R. Fischer, G. J. Matt, P. Feldner, T. Michel, A. Osvet, I. Levchuk, B. Merle, S. Golkar and H. Chen, *Nat. Photonics*, 2017, **11**, 436–440.
10 J. Pang, S. Zhao, X. Du, H. Wu, G. Niu and J. Tang, *Light: Sci. Appl.*, 2022, **11**, 105.
11 J. Zhao, L. Zhao, Y. Deng, X. Xiao, Z. Ni, S. Xu and J. Huang, *Nat. Photonics*, 2020, **14**, 612–617.
12 M. A. Green, E. D. Dunlop, J. Hohl-Ebinger, M. Yoshita, N. Kopidakis and X. Hao, *Prog. Photovoltaics*, 2020, **28**, 629–638.
13 D. Sirbu, F. H. Balogun, R. L. Milot and P. Docampo, *Adv. Energy Mater.*, 2021, **11**, 2003877.
14 L. Zhu, C. Chen, Y. Weng, F. Li and Q. Lou, *Sol. Energy Mater. Sol. Cells*, 2019, **198**, 11–18.
15 T. Bu, J. Li, F. Zheng, W. Chen, X. Wen, Z. Ku, Y. Peng, J. Zhong, Y.-B. Cheng and F. Huang, *Nat. Commun.*, 2018, **9**, 1–10.
16 K. Jung, J. Lee, C. Im, J. Do, J. Kim, W.-S. Chae and M.-J. Lee, *ACS Energy Lett.*, 2018, **3**, 2410–2417.
17 J. Wang, C. Song, Z. He, C. Mai, G. Xie, L. Mu, Y. Cun, J. Li, J. Wang and J. Peng, *Adv. Mater.*, 2018, **30**, 1804137.
18 S. Fang, B. Chen, B. Gu, L. Meng, H. Lu and C. M. Li, *Mater. Adv.*, 2021, **2**, 3629–3636.
19 H. Liu, S. Hussain, D. Vikraman, J. Lee, S. H. A. Jaffery, J. Jung, H.-S. Kim and J. Kang, *J. Alloys Compd.*, 2022, **906**, 164399.

20 Y. You, W. Tian, L. Min, F. Cao, K. Deng and L. Li, *Adv. Mater. Interfaces*, 2020, **7**, 1901406.

21 X. Yang, A. Wolcott, G. Wang, A. Sobo, R. C. Fitzmorris, F. Qian, J. Z. Zhang and Y. Li, *Nano Lett.*, 2009, **9**, 2331–2336.

22 K. Sivula, F. Le Formal and M. Grätzel, *ChemSusChem*, 2011, **4**, 432–449.

23 J. W. Lim, H. Wang, C. H. Choi, L. N. Quan, K. Chung, W.-T. Park, Y.-Y. Noh and D. H. Kim, *J. Power Sources*, 2019, **438**, 226956.

24 W. Hu, T. Liu, X. Yin, H. Liu, X. Zhao, S. Luo, Y. Guo, Z. Yao, J. Wang and N. Wang, *J. Mater. Chem. A*, 2017, **5**, 1434–1441.

25 C. Hou and H. Yu, *Chem. Eng. J.*, 2021, **407**, 127192.

26 S. Shabzendedar, A. R. Modarresi-Alam, M. Noroozifar and K. Kerman, *Org. Electron.*, 2020, **77**, 105462.

27 J. Han, H. Kwon, E. Kim, D.-W. Kim, H. J. Son and D. H. Kim, *J. Mater. Chem. A*, 2020, **8**, 2105–2113.

28 M. Naguib, M. W. Barsoum and Y. Gogotsi, *Adv. Mater.*, 2021, **33**, 2103393.

29 P. Das and Z.-S. Wu, *J. Phys.: Energy*, 2020, **2**, 032004.

30 C. Hou, H. Yu and C. Huang, *J. Mater. Chem. C*, 2019, **7**, 11549–11558.

31 L. Yang, Y. Dall'Agnese, K. Hantanasirisakul, C. E. Shuck, K. Maleski, M. Alhabeb, G. Chen, Y. Gao, Y. Sanehira and A. K. Jena, *J. Mater. Chem. A*, 2019, **7**, 5635–5642.

32 L. Nian, K. Gao, F. Liu, Y. Kan, X. Jiang, L. Liu, Z. Xie, X. Peng, T. P. Russell and Y. Ma, *Adv. Mater.*, 2016, **28**, 8184–8190.

33 Y. Guo, T. Liu, N. Wang, Q. Luo, H. Lin, J. Li, Q. Jiang, L. Wu and Z. Guo, *Nano Energy*, 2017, **38**, 193–200.

34 X. Liu, X. Li, Y. Li, C. Song, L. Zhu, W. Zhang, H. Q. Wang and J. Fang, *Adv. Mater.*, 2016, **28**, 7405–7412.

35 S. H. Liao, H. J. Jhuo, Y. S. Cheng and S. A. Chen, *Adv. Mater.*, 2013, **25**, 4766–4771.

36 K. I. Jayawardena, R. Rhodes, K. K. Gandhi, M. R. Prabhath, G. D. M. Dabera, M. J. Beliatis, L. J. Rozanski, S. J. Henley and S. R. P. Silva, *J. Mater. Chem. A*, 2013, **1**, 9922–9927.

37 M. K. Mohammed and M. Shekargoftar, *Sustainable Energy Fuels*, 2021, **5**, 540–548.

38 M. M. Tavakoli, R. Tavakoli, P. Yadav and J. Kong, *J. Mater. Chem. A*, 2019, **7**, 679–686.

39 Y. Wang, P. Xiang, A. Ren, H. Lai, Z. Zhang, Z. Xuan, Z. Wan, J. Zhang, X. Hao and L. Wu, *ACS Appl. Mater. Interfaces*, 2020, **12**, 53973–53983.

40 S. Hussain, D. Vikraman, M. T. Mehran, M. Hussain, G. Nazir, S. A. Patil, H.-S. Kim and J. Jung, *Renewable Energy*, 2022, **185**, 585–597.

41 S. Hussain, I. Rabani, D. Vikraman, T. Mehran, F. Shahzad, Y. S. Seo, H. S. Kim and J. Jung, *Int. J. Energy Res.*, 2021, **45**, 18770–18785.

42 S. Hussain, D. Vikraman, Z. A. Sheikh, M. T. Mehran, F. Shahzad, K. M. Batoo, H.-S. Kim, D.-K. Kim, M. Ali and J. Jung, *Chem. Eng. J.*, 2023, **452**, 139523.

43 D. Vikraman, S. Hussain, L. Hailiang, K. Karuppasamy, P. Sivakumar, P. Santhoshkumar, J. Jung and H.-S. Kim, *Inorg. Chem. Front.*, 2022, **9**, 5903–5916.

44 S. Hussain, H. Liu, M. Hussain, M. T. Mehran, H. S. Kim, J. Jung, D. Vikraman and J. Kang, *Int. J. Energy Res.*, 2022, **46**, 12485–12497.

45 C. Guo, Y. Hu, H. Qian, J. Ning and S. Xu, *Mater. Charact.*, 2011, **62**, 148–151.

46 Á. d. J. Ruíz-Baltazar, N. Méndez-Lozano, D. Larrañaga-Ordáz, S. Y. Reyes-López, M. A. Z. Antuñano and R. P. Campos, *Processes*, 2020, **8**, 946.

47 S. Majumder, S. Dey, K. Bagani, S. K. Dey, S. Banerjee and S. Kumar, *Dalton Trans.*, 2015, **44**, 7190–7202.

48 D. A. Tomalia, *J. Nanopart. Res.*, 2009, **11**, 1251–1310.

49 A. Sharma, B. Singh, S. Dhar, A. Gondorf and M. Spasova, *Surf. Sci.*, 2012, **606**, L13–L17.

50 L. Xu, M.-L. Yin and S. F. Liu, *Sci. Rep.*, 2014, **4**, 6745.

51 R. Zhang, P.-G. Yin, N. Wang and L. Guo, *Solid State Sci.*, 2009, **11**, 865–869.

52 R. F. Zhuo, H. T. Feng, Q. Liang, J. Z. Liu, J. T. Chen, D. Yan, J. J. Feng, H. J. Li, S. Cheng, B. S. Geng, X. Y. Xu, J. Wang, Z. G. Wu, P. X. Yan and G. H. Yue, *J. Phys. D: Appl. Phys.*, 2008, **41**, 185405.

53 M. Han, X. Yin, H. Wu, Z. Hou, C. Song, X. Li, L. Zhang and L. Cheng, *ACS Appl. Mater. Interfaces*, 2016, **8**, 21011–21019.

54 W. Y. Chen, X. Jiang, S.-N. Lai, D. Peroulis and L. Stanciu, *Nat. Commun.*, 2020, **11**, 1–10.

55 M. Mullet, V. Khare and C. Ruby, *Surf. Interface Anal.*, 2008, **40**, 323–328.

56 M. O. Amin, B. D'Cruz, M. Madkour and E. Al-Hetlani, *Microchim. Acta*, 2019, **186**, 1–10.

57 D. Vikraman, H. J. Park, S.-I. Kim and M. Thaiyan, *J. Alloys Compd.*, 2016, **686**, 616–627.

58 V. Dhanasekaran, T. Mahalingam, R. Chandramohan, J. K. Rhee and J. P. Chu, *Thin Solid Films*, 2012, **520**, 6608–6613.

59 J. Lin, Y. Yu, Z. Zhang, F. Gao, S. Liu, W. Wang and G. Li, *Adv. Funct. Mater.*, 2020, **30**, 1910479.

60 M. R. Habib, H. Li, Y. Kong, T. Liang, S. M. Obaidulla, S. Xie, S. Wang, X. Ma, H. Su and M. Xu, *Nanoscale*, 2018, **10**, 16107–16115.

61 A. Y. Kobitski, R. Scholz, D. R. T. Zahn and H. P. Wagner, *Phys. Rev. B: Condens. Matter Mater. Phys.*, 2003, **68**, 155201.

62 K. Mahmood, B. S. Swain and A. Amassian, *Adv. Energy Mater.*, 2015, **5**, 1500568.

63 F. Zhu, J. Hu, I. Matulionis, T. Deutsch, N. Gaillard, A. Kunrath, E. Miller and A. Madan, *Philos. Mag.*, 2009, **89**, 2723–2739.

64 H. Liu, S. Hussain, Z. Abbas, J. Lee, S. H. A. Jaffery, J. Jung, H.-S. Kim, D. Vikraman and J. Kang, *ACS Appl. Mater. Interfaces*, 2022, **14**, 33626–33640.

65 D. Vikraman, S. Hussain, H. Liu, S. H. A. Jaffery, K. Karuppasamy, J.-H. Lee, A. Kathalingam, J. Jung and

H.-S. Kim, *J. Mater. Res. Technol.*, 2022, **17**, 2875–2887.

66 Y. Kim, S. A. Choulis, J. Nelson, D. D. C. Bradley, S. Cook and J. R. Durrant, *Appl. Phys. Lett.*, 2005, **86**, 063502.

67 Z. Zhu, C. C. Chueh, F. Lin and A. K. Y. Jen, *Adv. Sci.*, 2016, **3**, 1600027.

68 F. Xia, Q. Wu, P. Zhou, Y. Li, X. Chen, Q. Liu, J. Zhu, S. Dai, Y. Lu and S. Yang, *ACS Appl. Mater. Interfaces*, 2015, **7**, 13659–13665.

69 H. Seon, D. Ban and J. Kang, *J. Instrum.*, 2018, **13**, C11009.

70 H. Liu, S. Hussain, J. Lee, D. Vikraman and J. Kang, *Materials*, 2021, **14**, 3206.